



OPEN Mechanistic analysis of frost heave in airport runway subgrades in seasonal frost regions and pavement structural tolerance thresholds

Chongwei Huang¹, Jinyang Liu¹ & Shanshan Wang²✉

This study addresses the structural damage of airport pavements caused by uneven frost heave in seasonal frozen soil regions. A three-dimensional finite element model based on elastic layered system theory was established to simulate pavement mechanical responses under various frost heave parameters (heave magnitudes: 5–30 mm, wavelengths: 6–20 m). Key findings reveal that: (a) The bending tensile stress at slab bottom in frost valley areas significantly exceeds that in frost peak regions, with maximum stresses concentrated at frost valley boundaries (2.466 MPa at slab top) and centers (2.531 MPa at slab bottom); (b) Both frost heave magnitude and wavelength exhibit linear positive correlations with pavement stress, while void areas expand with increasing parameters. Through fatigue stress calculations and specification validation, frost heave control criteria were proposed: permissible heave magnitudes of 20 mm for airports with Flight Area Code II A/B and 15 mm for Code II C-F facilities. The research establishes quantitative guidelines for frost-resistant pavement design in cold regions, effectively mitigating structural damage risks and extending pavement service life. This work fills the gap in the mechanical analysis of frost heave in airport pavements, providing theoretical support for infrastructure durability optimization and aviation safety enhancement in seasonal frozen soil areas.

Keywords Seasonal frozen soil, Airport subgrade, Frost heave index, Pavement structure model, Mechanical behavior

Seasonal frozen soil is widely distributed in mid-to-high latitude regions globally, particularly in northern China. During winter, the frost heave phenomenon in seasonal frozen soil causes uneven uplift of airport subgrades, while spring thawing leads to reduced subgrade density, pavement structure settlement, deformation, and voids under the slab. These phenomena not only cause pavement slab's cracks and even fractures but also severely impact airport operational safety. Therefore, the construction and maintenance of airports in seasonal frozen soil areas face significant challenges. However, current research lacks studies on the mechanical behavior of pavements under subgrade frost heave conditions. This paper uses numerical simulation methods to study the mechanical behavior of pavements under subgrade frost heave conditions in seasonal frozen soil areas and proposes frost heave control indicators for airport subgrades. The research findings on the mechanical behavior of pavements under frost heave conditions and the frost heave control indicators and standards can provide theoretical support for the anti-frost design of airports in seasonal frozen soil areas and guide the design and maintenance of airport subgrades throughout their life cycle.

Currently, research on frost heave in airport subgrades in seasonally frozen regions remains relatively limited. Liu et al.¹ investigated the frost heave characteristics of gravel-soil pavement structures in alpine airport regions using finite element models. Lenngren et al.² and Zaremotekhasas et al.³ proposed novel methods for non-destructive detection of pavement frost heave and measurement of airport road frost heave using unmanned aircraft systems, respectively. Long et al.⁴ established an original indoor experimental model for simulating uneven frost heave in airport pavement structures and validated its effectiveness through experiments. Their

¹Department of Transportation Engineering, University of Shanghai for Science and Technology, Shanghai 200093, China. ²Pudong New Area, COMAC Shanghai Aircraft Manufacturing Co. Ltd, COMAC Building, 1919 Expo Avenue, Shanghai, No, China. ✉email: 1029761683@qq.com

work visually replicated slab-end fracture phenomena between runway slabs and shoulders. However, studies focusing specifically on subgrade frost heave phenomena are more extensive.

Lai et al.⁵ proposed that frost heave primarily results from water migration from unfrozen zones to the freezing front. The occurrence of frost heave requires three fundamental conditions: Frost-susceptible soils (typically fine-grained soils), freezing temperatures, and water supply to the freezing front, with frost heave frequently observed in areas with sufficient water availability. Wang et al.⁶ highlighted that frost heave and thaw settlement in seasonal frozen soils directly affect the stability of engineering foundations in cold regions, with freezing duration emerging as a key factor influencing frost heave.

Currently, finite element methods have become a significant approach for simulating frost heave formation in seasonal frozen soil regions. Sun et al.⁷ developed a three-dimensional freezing model based on the finite-discrete element method, capable of simulating frost heave processes involving heat transfer, water migration, water-ice phase transitions, and ice-rock interactions. Teng et al.⁸ combined experimental evidence and numerical simulations to investigate frost heave caused by vapor transfer in coarse-grained soils. This study provided the first experimental or numerical evidence in this field, but its applicability to other soil types requires further research. Cheng et al.⁹ explored classification, deconstruction, and evaluation methods for frost heave models, analyzing simulation errors arising from modeling approaches. Ye et al.¹⁰ proposed an innovative interdisciplinary thermal-hydro-mechanical fractal model for quantitatively studying microstructure effects on frost heave, though further validation is needed for practical engineering applications.

Research on frost heave in railway subgrades holds significant reference value for airport runway subgrade studies. Zhang et al.¹¹ experimentally investigated the frost heave characteristics and microscopic mechanisms of fine-grained soils in heavy-haul railway subgrades under dynamic loads in seasonal frozen soil areas. However, this study was limited to heavy railway subgrades in seasonal frozen soil areas, requiring further research on other soil types or loading conditions. Hou et al.¹² examined the frost heave properties of high-speed railway subgrade fill materials in seasonal frozen soil areas through laboratory tests, but real-world engineering validation remains necessary. Lee et al.¹³ calculated frost penetration depths and frost heave in concrete railroad tracks during construction. Fattoev et al.¹⁴ revealed fundamental characteristics of soil frost heave in railway engineering. Innovations in material modification and structural reinforcement technologies enable us to address pavement distress using higher-performance materials. Jin et al.¹⁵ proposed rubber-modified asphalt, characterized by its lower fracture stress at low temperatures, making it highly suitable for anti-freeze applications in pavements. Concurrently, Li et al.¹⁶ investigated two transverse reinforcement methods for PCB bridges and validated them through finite-element modeling. This methodology provides critical insights for developing finite-element models of aircraft runways in similar contexts.

Despite many researchers proposing their understanding of how to address frost heave, there is still a gap in research on the frost heave patterns and control indicators for airport subgrades in seasonal frozen soil areas. The studies have made significant progress in understanding and mitigating frost heave, but they may not fully address the issues of airport runways under frost heave conditions. Airport runways have unique characteristics that differ from other roads, and many studies focus on general soils or railway applications rather than the specific conditions and requirements of airport runways.

To address these issues, this paper employs finite element software to establish a pavement structure model based on the frost heave state of the subgrade. The study investigates the impact of the subgrade frost heave state under self-weight on the mechanical behavior of the pavement and proposes frost heave control indicators based on the influence on the pavement's mechanical behavior.

Construction of pavement structure model based on frost heave conditions

Using the relevant finite element software and based on the theory of elastic layered systems, this study determines the geometric dimensions of airport pavement structures (surface layer, base layer, and subgrade) and sets the material properties of each structural layer. Considering factors such as frost heave amount, frost heave wavelength, and relative position of frost heave in the subgrade, and based on field monitoring data and literature review results, the frost heave amount and wavelength are determined, and the frost heave simulation method is established to construct a pavement structure model based on frost heave conditions.

Finite element motion equations and solutions for pavement

The core concept of finite element analysis (FEA) is to decompose a large structural model into several small elements that are interconnected at nodes. This process involves using predefined approximate functions within each small element to segmentally approximate the function over the entire solution domain. Through this method, the originally continuous dynamic problem with infinite degrees of freedom is transformed into a discrete problem with finite degrees of freedom. As the number of elements increases, the approximate solution gradually approaches the true solution, but the required computational resources and time also increase correspondingly.

Motion equations

Based on the mechanical model of airport runways, combined with the basic assumptions of a multi-layer elastic system and the fundamental principles of elastic dynamics, the finite element dynamic analysis equation of airport runway structures under moving loads can be derived as follows:

$$\{F_i\} + \{F_d\} + \{F(t)\} = \{F_e\} \quad (1)$$

$$\{F_i\} = -[M] \frac{\partial^2 \{\delta\}}{\partial t^2} = -[M] \{\ddot{\delta}\} \quad (2)$$

$$\{F_d\} = -[C] \frac{\partial \{\delta\}}{\partial t} = -[C] \{\dot{\delta}\} \quad (3)$$

$$\{F_e\} = [K] \{\delta\} \quad (4)$$

where:

($\{F_i\}$) represents the inertial force, ($\{F_d\}$) represents the damping force, ($\{F_e\}$) represents the elastic force. Substituting these forces into the total equation, we get

$$[M] \{\ddot{\delta}\} + [C] \{\dot{\delta}\} + [K] \{\delta\} = \{F(t)\} \quad (5)$$

where:

($[M]$) is the mass matrix of the pavement, ($[C]$) is the damping matrix of the pavement, ($[K]$) is the stiffness matrix of the pavement, ($\{\ddot{\delta}\}$) is the acceleration (m/s²), ($\{\dot{\delta}\}$) is the velocity (m/s), ($\{\delta\}$) is the displacement (m), ($\{F(t)\}$) is the dynamic load of the aircraft (kN).

Stiffness matrix The element stiffness matrix ($[k_{rs}]$) can be expressed as:

$$[k_{rs}] = [B_r]^T [D] [B_s] tA \quad (6)$$

where:

($[k_{rs}]$) is the strain matrix, ($[B]$) is the strain matrix, ($[D]$) is the elasticity matrix, (t) is the element thickness (m), (A) is the element area (m²).

The element stiffness matrix can be written in blocks as:

$$[k]^e = \begin{bmatrix} k_{ii} & k_{ij} & k_{im} \\ k_{ji} & k_{jj} & k_{jm} \\ k_{mi} & k_{mj} & k_{mm} \end{bmatrix} \quad (7)$$

where ($[k_{rs}]$) is a 2×2 matrix:

$$[k_{rs}] = [B_r]^T [D] [B_s] tA = \begin{bmatrix} k_{rs}^1 & k_{rs}^2 \\ k_{rs}^3 & k_{rs}^4 \end{bmatrix} \quad (8)$$

The overall stiffness of the structure can be obtained by assembling the element stiffness matrices.

Unit mass matrix First, using D'Alembert's principle to discretize the structure, the load-moving formula is then substituted into the solution process. For a small element of the zero-structure, based on D'Alembert's principle, the inertial force per unit volume can be derived as follows:

$$\{P_i\} = \rho_0 \frac{\partial^2 \{u\}}{\partial t^2} \quad (9)$$

where: (u) is the displacement (m), (ρ_0) is the material density (kg/m³).

After discretizing the structure, the displacement function for a small element can be expressed as:

$$\{u\} = [N] \{\delta\}^e \quad (10)$$

where (N) is the shape function. Substituting Eq. (10) into Eq. (9), we get:

$$\{P_i\} = \rho_0 [N] \frac{\partial^2 \{\delta\}^e}{\partial t^2} \quad (11)$$

Using the general formula for moving loads:

$$\{P\}_q^e = \iiint [N]^T \{P_i\} dx dy dz \quad (12)$$

Substituting Eq. (11) into Eq. (12), the inertial force at the element nodes can be obtained as:

$$\begin{aligned} \{F_i\}^e &= \int [N]^T \{P_i\} dV \\ &= \int [N]^T \rho_0 [N] \frac{\partial^2 \{\delta\}^e}{\partial t^2} dV \\ &= \int [N]^T \rho_0 [N] dV \frac{\partial^2 \{\delta\}^e}{\partial t^2} \end{aligned} \quad (13)$$

From Eq. (13), the element mass matrix can be seen as:

$$\{M\} = \int [N]^T \rho [N] dV \quad (14)$$

Damping matrix For a small element in the structure, the damping force per unit volume is:

$$\{P_d\} = a\rho_0 \frac{\partial \{u\}}{\partial t} = a\rho_0 [N] \frac{\partial \{u\}^e}{\partial t} \quad (15)$$

where (a) is the proportional function. Using the general formula for moving loads (21) and substituting Eq. (15), we get:

$$\begin{aligned} \{F_i\}^e &= \int [N]^T \{P_d\} dV \\ &= a \int [N]^T \rho_0 [N] \frac{\partial^2 \{\delta\}^e}{\partial t^2} dV \\ &= a \int [N]^T \rho_0 [N] dV \frac{\partial^2 \{\delta\}^e}{\partial t^2} \end{aligned} \quad (16)$$

From Eq. (16), the element damping matrix can be obtained as:

$$\{c\} = a[[N]^T \rho_0 [N] dV = a[M] \quad (17)$$

From Eq. (17), the element damping matrix is proportional to the mass matrix. Assuming the damping force is proportional to the strain rate, the damping force can be expressed as:

$$\begin{aligned} \{F_d\}^e &= \int [B]^T [D] \{\sigma_0\} dV \\ &= \beta \int [B]^T [D] [B] dV \frac{\partial \{\delta\}^e}{\partial t} \\ &= [c] \frac{\partial \{\delta\}^e}{\partial t} \end{aligned} \quad (18)$$

$$[c] = \beta [[B]^T [D] [B] dV = \beta [K] \quad (19)$$

s proportional to the stiffness matrix. In practical calculations, the damping matrix is obtained for the overall structure, generally using Rayleigh damping:

$$[C] = a[M] + \beta[K] \quad (20)$$

Solving the motion equations

In the field of dynamic numerical analysis, strategies for solving ordinary differential equations are generally divided into direct integration methods and mode superposition methods. Direct integration methods can handle various problems, including nonlinear ones, while mode superposition methods are typically limited to linear problems. Since this study deals with a nonlinear problem, the direct integration method is chosen for computation. Direct integration methods include the central difference method, Newmark- β method, and Wilson- θ method. The mathematical expressions are as follows:

$$\{\ddot{\delta}\} = \frac{1}{\Delta t^2} (\delta_{t-\Delta t} - 2\delta_t + \delta_{t+\Delta t}) \quad (21)$$

$$\{\dot{\delta}\} = \frac{1}{2\Delta t} (\delta_{t+\Delta t} - \delta_{t-\Delta t}) \quad (22)$$

Substituting Eqs. (21) and (22) into the motion equation, we get:

$$\left(\frac{1}{\Delta t^2} + \frac{1}{2\Delta t}C\right) \delta_{t+\Delta t} = F_t - \left(K - \frac{2}{\Delta t^2}M\right) \delta_t - \left(\frac{1}{\Delta t^2}M - \frac{1}{2\Delta t}C\right) \delta_{t-\Delta t} \quad (23)$$

From Eq. (23), the solution at each discrete time point is obtained using a recursive formula, where the time step (Δt) must satisfy the following conditions:

$$\begin{cases} \Delta t \leq \Delta t_{cr} = \frac{T_n}{\pi} \left(\sqrt{1 + \xi^2} - \xi \right), & \text{with damping} \\ \Delta t \leq \Delta t_{cr} = \frac{T_n}{\pi}, & \text{without damping} \end{cases}$$

Model establishment and frost heave simulation

Mesh division and boundary conditions

The software used includes various types of three-dimensional solid elements, as shown in the figure, considering the running time and the performance of each solid unit, this project selects C3D8R hexahedral solid element, C represents the body element, 3D represents the three-dimensional element, 8 represents eight nodes, R represents reduced reduction integral, that is, eight-node linear hexahedral element. This unit is the least time-consuming hexahedral element in the finite element software, and the calculation accuracy of the hexahedron itself is higher than that of tetrahedron and chisel element, so C3D8R is the most widely used in the practical application of the bulk element, so this project simulates the surface layer, base layer and soil foundation in the pavement structure, The solid unit is shown in the Fig. 1.

Mesh Division: To ensure simulation accuracy while considering computational efficiency, this study uses a mesh size of $0.2 \times 0.2 \times 0.2$ m for the surface and base layers, and a larger mesh size of $0.6 \times 0.6 \times 0.6$ m for the

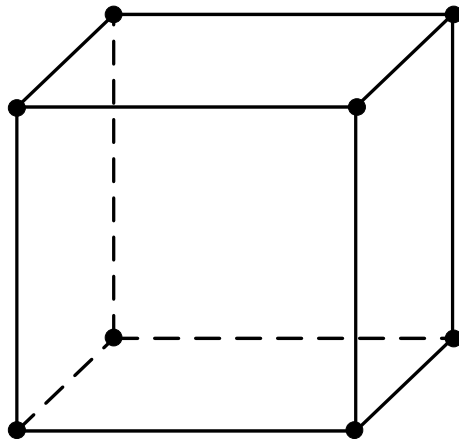


Fig. 1. C3D8R unit structure.

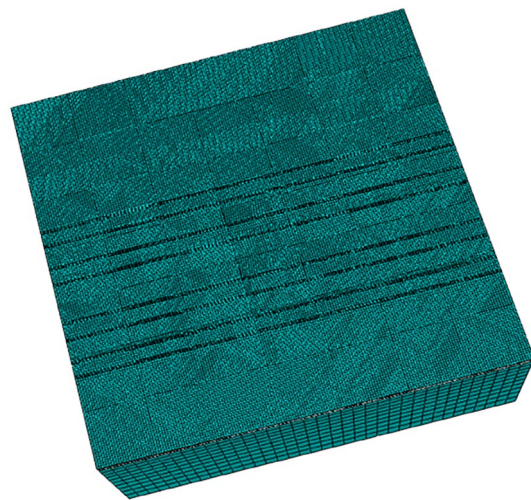


Fig. 2. Schematic diagram of grid division of pavement structure model.

foundation. To improve the accuracy of the region under aircraft load, local mesh refinement is applied to the surface and base layers, The grid distribution is shown in the Fig. 2.

Geometric model

The airport runway mainly consists of two parts: the surface pavement structure and the underlying subgrade soil. According to the materials used in the pavement structure, the runway can be divided into two types: rigid and flexible. As shown in Fig. 3, this project focuses on the rigid pavement structure, specifically the cement concrete pavement structure. No cushion layer is set, and the pavement model includes a cement concrete surface layer, a cement-stabilized gravel base layer, and a subgrade.

This project mainly constructs the airport pavement model based on the linear elastic model and the elastic layered system theory. As shown in Fig. 4 when calculating the problem of cement concrete pavement structure, since the pavement layers are composed of different materials with different characteristics, the pavement structure can be regarded as an elastic layered system with a uniformly distributed load on the surface layer.

Therefore, the calculation model is established based on the following assumptions:

- (1) The materials of the pavement structural layers are all set as elastic bodies, and the contact between the pavement structural layers is continuous;
- (2) The frost heave amount of the airport pavement structure is set on the top surface of the subgrade. Since the surface and base layers have low water content when the structure is intact, the materials of the surface and base layers are set to not undergo frost heave (frost heave coefficient is 0);
- (3) The pavement structure model is constructed based on the final shape of the frost heave deformation of the subgrade. The frost heave shape of the subgrade is the result of the coupling effect of the temperature field and the moisture field. This project does not consider the frost heave deformation process of the subgrade

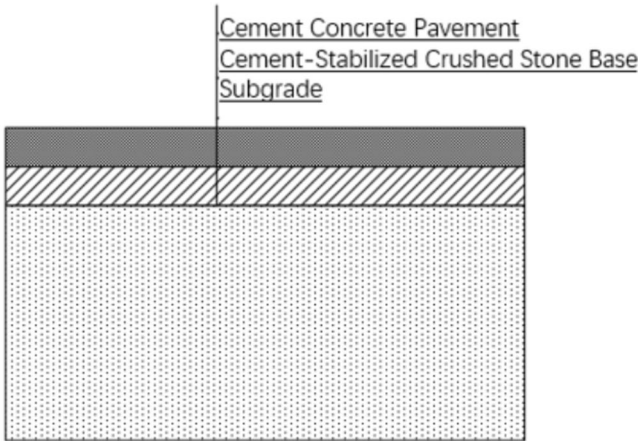


Fig. 3. Airport cement concrete pavement structural layer.

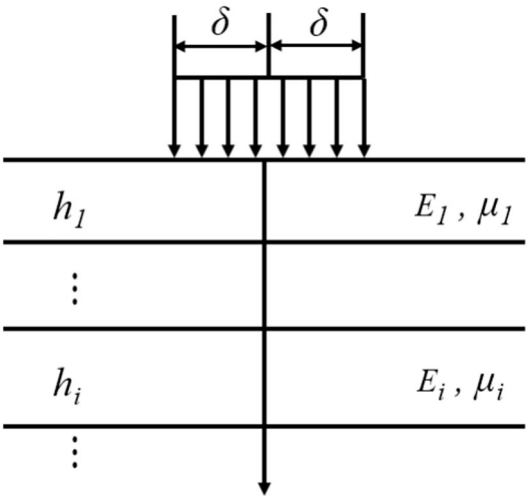


Fig. 4. Elastic layered system.

Airport Structural Layer	thickness(cm)	Poisson's ratio	density(kg/m ³)	Elastic modulus (MPa)	damping
Cement concrete surface course	40	0.15	2400	36,000	0.8
Base layer (cement stabilized gravel layer)	40	0.25	2100	1500	0.8
Soil	1420	0.35	1920	60	0.4

Table 1. Pavement structure material parameters.

- in numerical simulation, and does not set the temperature field and moisture field, only calculating the mechanical response of the pavement structural layers under self-weight and aircraft load;
- (4) The frost heave shape of the subgrade is set based on the parameters of frost heave amount and frost heave wavelength.

Model material parameters

According to the “Design Specifications for Cement Concrete Pavement of Civil Airports” (MHT5004-2010), the design requirements for the surface and base layers of airport runways are shown in Table 1.

The pavement slab size in this project is set to 5 m × 5 m, with a 10 mm joint between slabs. The structural thickness of the model is taken as 8 m, so the total thickness of the pavement structure and subgrade is determined to be 15 m based on actual analysis needs. Considering that the runway width of most trunk airports in China is generally around 45 m, this project comprehensively considers the computing power and accuracy

Virtual material modulus (MPa)	Load transfer factor of the seam (%)	Load transfer capacity rating criteria
> 80	> 80	Good
10 ~ 80	56 ~ 80	middle
5 ~ 10	31 ~ 55	times
< 5	< 30	difference

Table 2. Correspondence between modulus of virtual materials and load transfer capacity of joints.

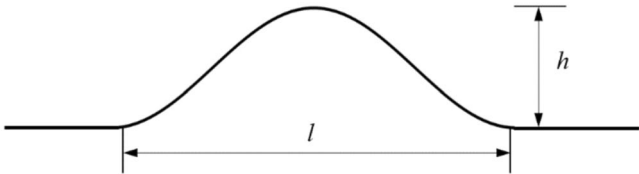


Fig. 5. Frost heave deformation diagram of cosine type base.

requirements, combined with the research objectives of this project, and sets the total width of the pavement to 35.06 m and the total length to 35.06 m.

To simplify the model, this project uses the virtual material layer method to simulate the joints between slabs. The thin layer width is the same as the joint width, and the length and thickness are the same as the pavement slab. Based on the evaluation standard of the load transfer capacity of cement concrete pavement joints, the correspondence between the virtual material modulus and the load transfer capacity of the joint is shown in Table 2. Considering the load transfer capacity of transverse and longitudinal joints is 91%, the elastic modulus of the joint material is set to 600 MPa, Poisson’s ratio is 0.25, and density is 2100 kg/m³.

Considering the running time and performance of each solid element, this project selects the C3D8R hexahedral solid element.

The contact relationship between the surface layer and the base layer and the base layer and the soil foundation is simulated in the tangential direction, and the hard contact simulation is used in the normal direction.

Basis for frost heave simulation

Track irregularity induced by subgrade displacement is conventionally modeled as a cosine curve^{17,18}. Given the experimental track irregularity data from frost-heave regions of railway subgrades documented in⁹, modeling frost-heave displacement using a cosine function is considered reasonable.

The convex cosine curve shown in Fig. 5 can be used to represent the frost heave shape on the surface of the subgrade. Thus, the frost heave shape is mainly described by two parameters: Frost heave amount and frost heave wavelength.

The expression for the longitudinal frost heave deformation along the subgrade is as follows:

$$y = \begin{cases} h[\frac{1}{2} - \frac{1}{2}\cos(\frac{2\pi Z}{l})] & Z \in \text{frost heave area} \\ 0 & Z \in \text{Non - frost heave zone} \end{cases} \tag{24}$$

where, *h*—Total frost heave volume, mm;

Z—The coordinates of the subgrade surface along the longitudinal position of the line;
—Frost heave wavelength, m.

The distribution range of subgrade frost heave amount in seasonal frozen areas is concentrated between 5-20 mm, and the distribution range of frost heave wavelength is concentrated between 6-20 m. Therefore, this project proposes frost heave control standards based on the frost heave amount, setting the simulated frost heave amount between 5-30 mm and the frost heave wavelength between 6-20 m.

Frost heave simulation method

Frost heave of the subgrade leads to the formation of frost valleys and frost peaks on the subgrade surface, resulting in discontinuous void areas under the base layer. These void areas, due to the loss of continuous contact with the foundation, cannot effectively transfer forces and displacements, thereby weakening the bearing capacity of the foundation. In finite element analysis, this void phenomenon can generally be simulated by adjusting the foundation reaction modulus of the void area to accurately reflect its impact on the overall structural performance. To simplify the model, This project simulates frost heave valleys and peaks by cutting the subgrade in finite element software.

As shown in Fig. 6, the frost heave area is set as a square with the wavelength as the side length on the subgrade plane, and the overall shape of the frost valley is set as a quadrangular pyramid.

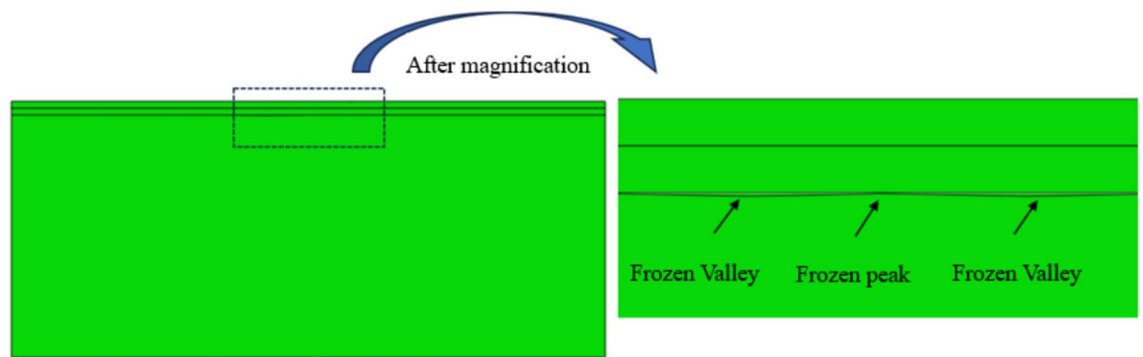


Fig. 6. Schematic diagram of frost heave simulation section of pavement.

Aircraft load model

Load application methods

Aircraft STATIC Load In accordance with airport design specifications, aircraft loads are typically simplified as static loads. The load magnitude is determined based on the aircraft type, and the load expression at a distance r from the load center is as follows:

$$P = \begin{cases} P_0, & |r| \leq |r_0| \\ 0, & |r| > |r_0| \end{cases} \quad (25)$$

where:

P_0 —Uniform load, kN;

r_0 —Distance from the load center to the distribution boundary, m.

Load application methods In current research, simulations of aircraft moving loads can be categorized into moving constant loads and moving vibration loads. The moving constant load simplifies aircraft load as a constant load moving along the taxiing direction, achieving load mobility while maintaining unchanged magnitude. Building upon the moving constant load framework, vibration frequency and amplitude are introduced to more realistically reflect the dynamic effects of aircraft operation.

For simulating moving vibration loads, two primary methodologies are typically employed:

Random vibration load simulation : This approach better captures the actual dynamic loads encountered during aircraft operation. However, it necessitates extensive field measurements and statistical analysis due to uncertainties in aircraft type, taxiing speed, and runway surface irregularities, rendering the modeling process complex and resource-intensive.

Steady-state sinusoidal wave vibration load simulation: To streamline analysis, this project approximates aircraft moving load as a steady-state sinusoidal wave vibration load, expressed as:

$$P = P_j + P_d \quad (26)$$

where:

P_j = static load component (kN),

P_d = dynamic load component (kN).

Although simplified, this method effectively captures the primary dynamic characteristics of aircraft loads.

Load magnitude and contact area

The wheel load contact area is defined as the area covered when an aircraft tire contacts the supporting surface (pavement). According to current airport design specifications, the calculation of aircraft wheel load contact area is as follows:

$$L_t = \sqrt{\frac{P_t * 10^4}{5.227q}} \quad (27)$$

$$W_t = 0.6L_t \quad (28)$$

where:

q —Tire pressure of the main landing gear, MPa;

P_t —Wheel load on the main landing gear, MPa;

L_t —Tire imprint length, mm;

W_t —Tire imprint width, mm.

In finite element software simulations, model simplification is employed to balance computational accuracy and efficiency. As illustrated in Fig. 7, the tire contact area can be approximated as a rectangle while preserving the total contact area unchanged. This simplification serves as a rational approximation of the actual tire-pavement interaction, aiming to reduce computational complexity while ensuring result reliability.

Aircraft static load magnitude Aircraft load describes the overall force exerted by an aircraft on pavement, transmitted through its wheels. According to Chinese civil aviation specifications, the load on each wheel of the main landing gear is assumed to be equal. The load per single wheel is calculated as:

$$P_0 = \frac{\rho * G}{n_e} \quad (29)$$

where:

P_0 – Load per single wheel (kN); G – Total aircraft load (kN);

ρ – Load distribution coefficient of the main landing gear;

n_e – Total number of wheels on the main landing gear.

Different aircraft landing gear configurations exert distinct loading patterns on pavement surfaces. Common primary landing gear configurations include single-axle dual-wheel, dual-axle dual-wheel, triple-axle dual-wheel, and composite types. This project investigated three aircraft models representing different load gradients: the B767-300ER, B747-400, and A380-800. The landing gear configurations of these different aircraft are depicted in Fig. 8. Notably, the B747 series is the most numerous passenger aircraft in service, carrying over 50% of global air passenger traffic, while the A380-800 is currently the world's largest passenger aircraft.

Taking the A380-800 model as an example to calculate wheel loads, its main landing gear has a total of 20 wheels and a maximum taxi weight of 5620 kN. Applying the distribution coefficient to this maximum taxi weight allocates the load to the wheels of the main landing gear. Accordingly, the calculated single-wheel load is 267.23 kN. The single-wheel loads and wheel imprint sizes for the other aircraft models were similarly determined based on their respective maximum taxi weights, as listed in Table 3.

Magnitude of aircraft dynamic loads Aircraft activities on runways primarily comprise two states: taxiing before takeoff and after landing, both of which impose dynamic effects on the pavement. D0.

During accelerated taxiing for takeoff, the pressure exerted by aircraft on the runway decreases due to increased wing lift. Consequently, the load borne by the runway during takeoff is typically lower than during post-landing taxiing. Considering the impact of aircraft taxiing after landing, the dynamic loads generated include not only direct tire-ground contact loads but also dynamic effects induced by tire vibrations. To account for vibrational effects in calculations, this study amplifies the wheel load by 10% to simulate vibration impacts.

Given a wheel diameter d of 1.5 m and a taxiing speed v of 55 m/s (prior to deceleration after landing), the excitation frequency is calculated as follows:

$$f = \frac{v}{\pi d} \quad (30)$$

Substituting the values yields $f = 11.68$ Hz. The angular frequency ω is then derived from:

$$\omega = f * 2\pi \quad (31)$$

resulting in $\omega = 73$ rad/s. The dynamic load for a single main landing gear wheel is expressed as:

$$P_0' = P_0 + 10\%P_0 \sin(\omega t) \quad (32)$$

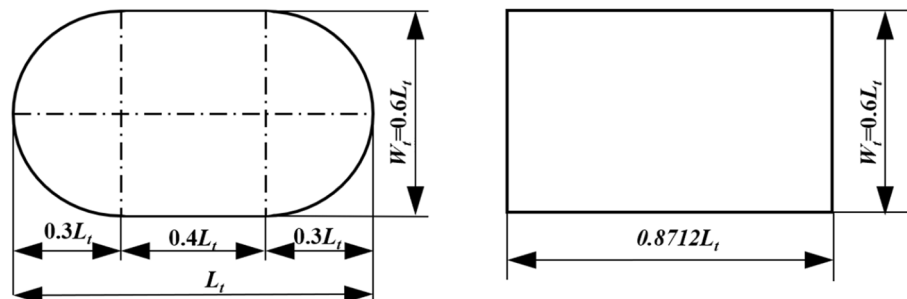


Fig. 7. Schematic diagram of the shape and equivalent of the wheel print.

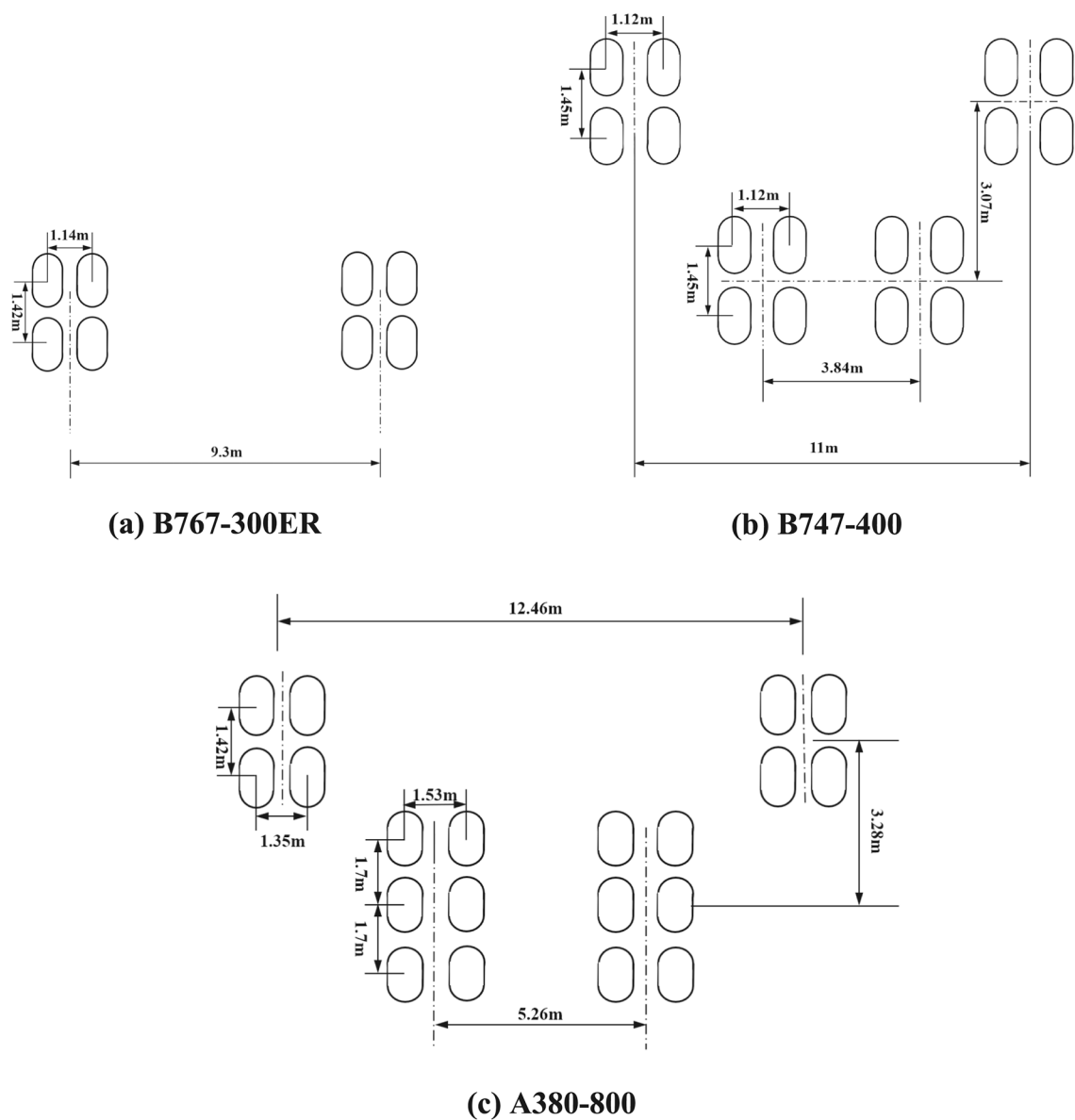


Fig. 8. Landing and landing architecture types of different models.

Models	B767-300ER	B747-400	A380-800
Maximum glide weight (kN)	1873	3978	5620
Main landing architecture type	Twin axle and double wheels	Twin axle and double wheels	Three-axle twin wheel/twin axle double wheel
Number of main landing gear ne (pcs)	2	4	4
Main landing gear single wheel load (kN)	222.42	236.69	267.23
Tire pressure (MPa)	1.38	1.38	1.47
The main landing gear load distribution coefficient p	0.95	0.952	0.951
Wheel printing length (m)	0.484	0.499	0.514
Wheel printing width (m)	0.333	0.344	0.354
Rotation area (m2)	0.161	0.172	0.182

Table 3. Main parameters of different models.

Based on load calculations, the static load for an A380-800 main landing gear single wheel is 267.23 kN. Substituting this into Eq. (8.13), the spatial distribution of the dynamic load for the A380-800 main landing gear single wheel can be determined.

Influence of frost heave state on pavement mechanical behavior under self-weight

Based on the previously established pavement structure model considering frost heave morphology of the subgrade, the mechanical behavior of the pavement surface layer at frost peaks and frost valleys under self-weight is analyzed to determine the critical stress locations on the pavement. Further analysis is conducted on the effects of frost heave amplitude, wavelength, and position on pavement stress and displacement.

Mechanical behavior of pavement at frost peaks and frost valleys

This section takes a frost heave amount of 10 mm and a wavelength of 6 m as an example. As shown in Fig. 9, frost peaks and frost valleys are set above the subgrade. The pavement stress in the frost peak and frost valley areas of the subgrade under self-weight is analyzed. The contour maps show that the maximum horizontal lateral stress and maximum horizontal longitudinal stress of the surface layer both appear at the bottom of the slab above the frost valley. This indicates that when frost heave occurs in the subgrade, the surface layer above the frost valley is subjected to greater bending tensile stress compared to the frost peak. Therefore, the pavement above the frost valley is in an unfavorable stress position. Further analysis is conducted on the mechanical effects of different frost heave amounts, wavelengths, and positions on the pavement.

Frost heave causes the soil to move upward. This movement originates from the expansion of accumulated water within the soil as it freezes. When ice lenses grow, the overlying soil and pavement surface can undergo “frost heaving”, potentially leading to cracking and roughness in the pavement. The stress concentration in frost troughs is a specific manifestation of this phenomenon. For airport runways, the high bending tensile stresses within these frost trough areas significantly increase the risk of pavement cracking. This is particularly true under the combined action of aircraft loads and frost heave deformations, because the non-uniform upward heaving of the soil lifts the pavement surface, inducing bending stresses within the asphalt layer. These bending stresses can lead to cracking. Therefore, we chose this area as the main research object.

Influence of frost heave morphology on pavement mechanical behavior

Based on monitoring results and related survey data, this section studies the influence of frost heave amount, wavelength, and position on pavement mechanical behavior. Four wavelengths (6 m, 10 m, 15 m, 20 m) and five frost heave amounts (10 mm, 15 mm, 20 mm, 25 mm, 30 mm) are selected for analysis. The relationship between frost heave wavelength and the relative position of the concrete slab is shown in Fig. 10.

Influence of frost heave amount on pavement stress

To study the influence of frost heave amount on pavement stress under self-weight, five frost heave amounts (10 mm, 15 mm, 20 mm, 25 mm, 30 mm) are selected, and each frost heave amount corresponds to three wavelengths (6 m, 10 m, 20 m) for numerical simulation. The pavement stress contour maps are shown in Fig. 11. The stress extraction path for each frost heave morphology is a path parallel to the x-axis passing through the center of the frost valley.

As shown in Fig. 12, the stress on the top plate is analyzed along a specified path to study the variation of horizontal stress with different frost heave amounts. The distribution pattern of horizontal stress along the top plate remains consistent across various frost heave amounts. At the frost valley, insufficient support beneath the surface layer causes the top plate to experience downward pressure due to self-weight, indicating compression in this region. Near the frost heave boundary, where the base layer provides adequate support, tensile forces arise from the pavement's gravity in the frost valley area, resulting in higher tensile stress on the top plate.

Further analysis reveals that:

- With a frost heave wavelength of 6 m, the maximum bending tensile stress on the top plate occurs within 0.9 to 1.2 m from the frost valley boundary.
- With a wavelength of 10 m, the maximum bending tensile stress appears within 0.5 to 1 m from the frost valley boundary.

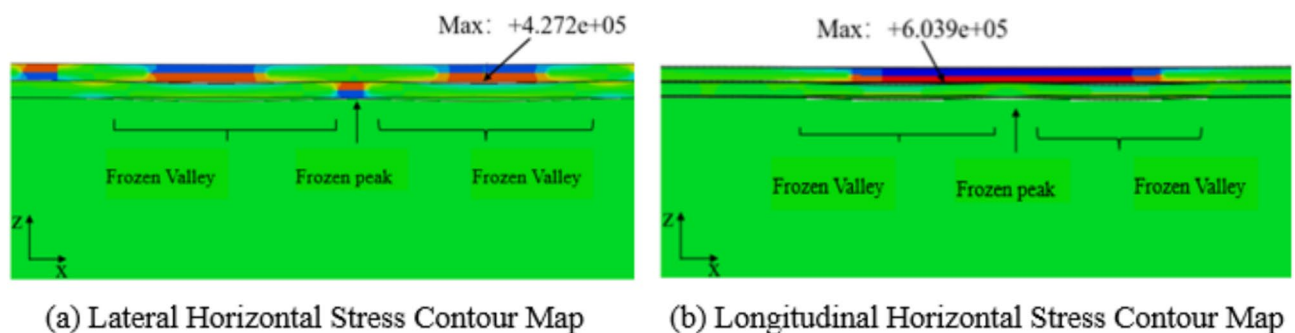


Fig. 9. Frost heave pavement horizontal stress contour map (Profile).

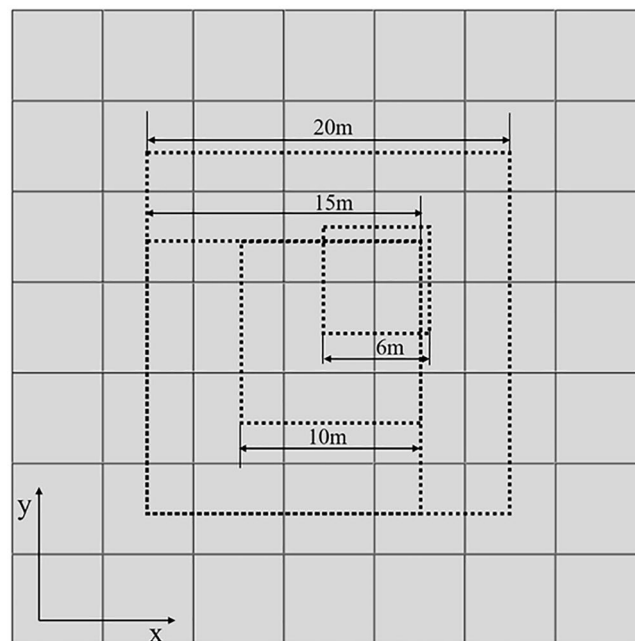


Fig. 10. Relationship between frost heave wavelength and panel relative position.

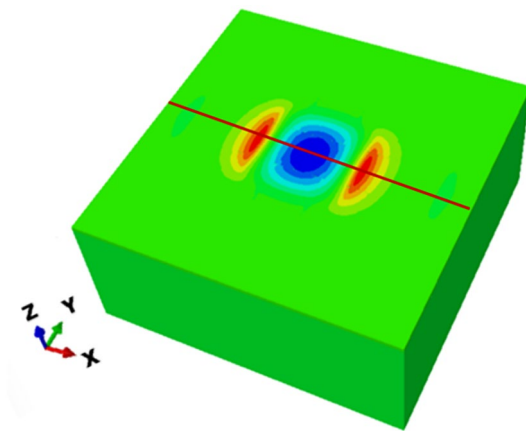


Fig. 11. Pavement lateral horizontal stress contour map (Wavelength 10 m).

- When the wavelength increases to 20 m, the maximum bending tensile stress is located exactly at the frost valley boundary.

Therefore, in cases of uneven frost heave in the subgrade, the area near the frost valley boundary on the top plate experiences the greatest bending tensile stress, making it the most critical stress point. As the wavelength increases, the location of maximum bending tensile stress on the top plate shifts closer to the frost valley boundary.

As shown in Fig. 13, the bottom plate stress is extracted along the path to study the variation of horizontal stress at the bottom plate with frost heave amount. Under different frost heave amounts, the distribution pattern of horizontal stress at the bottom plate with distance is the same. The bottom plate at the frost valley boundary is subjected to compressive stress due to gravity, while the bottom plate in the frost valley area is subjected to tensile stress due to loss of support. The maximum bending tensile stress appears at the center of the frost valley, making the bottom plate at the center of the frost valley the most unfavorable stress position.

Further analysis shows that as the frost heave amount increases, the compressive stress at the bottom plate at the frost valley boundary and the tensile stress at the bottom plate in the frost valley both show an increasing trend. This indicates that an increase in frost heave amount causes stress concentration. Additionally, when the wavelength is 20 m, this stress concentration becomes more significant with the increase in frost heave amount. This indicates that a larger wavelength combined with a larger frost heave amount is likely to cause unstable stress in the pavement structure, leading to damage. Summarize the data in the Fig. 14 into a Table 4.

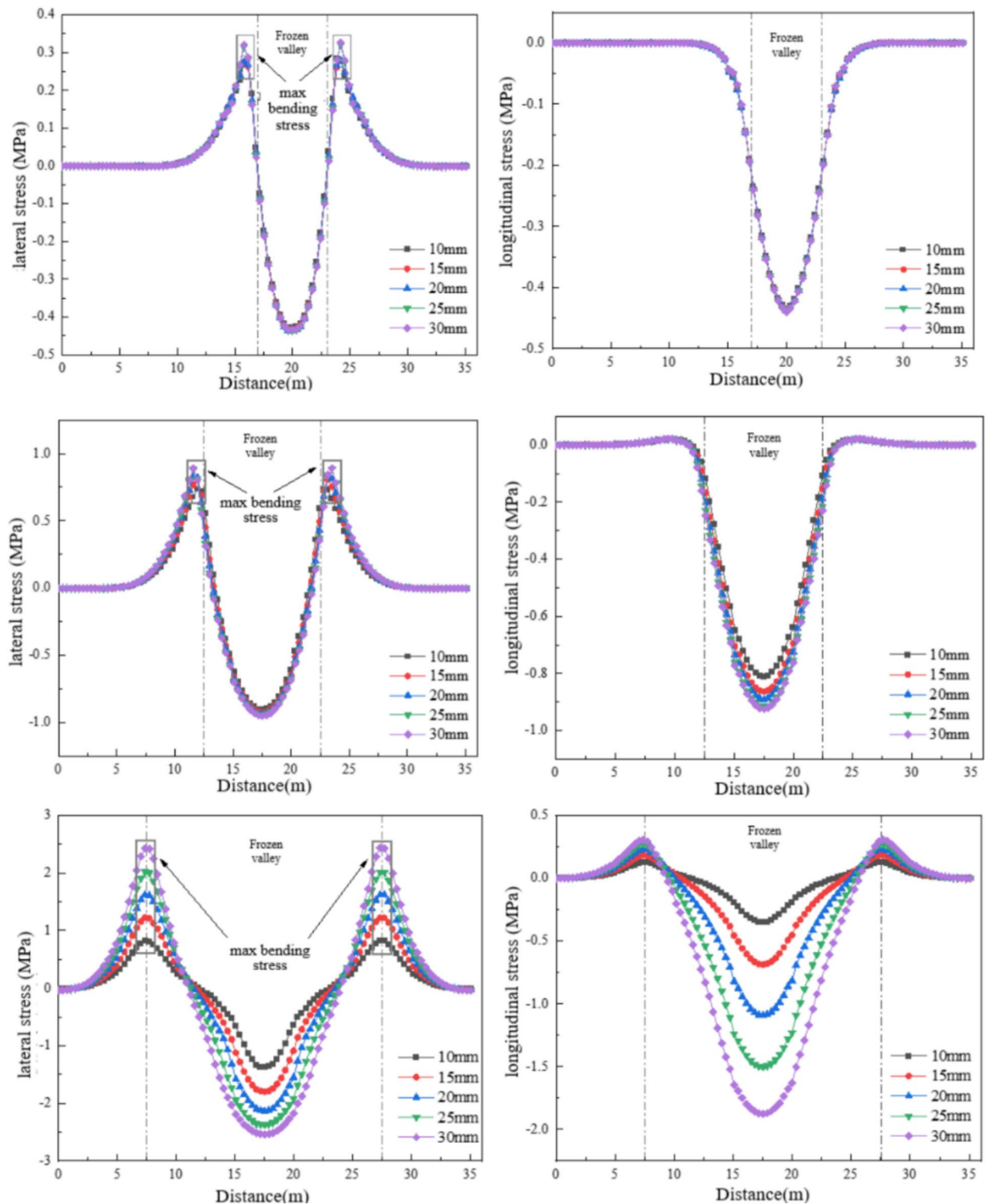


Fig. 12. Top plate horizontal stress (wavelength 6 m;10 m;20 m).

Therefore, the maximum bending tensile stress values at both the top and bottom plates are positively correlated with the frost heave amount. Under the same frost heave morphology, the bending tensile stress at the top plate is generally smaller than that at the bottom plate, and the increase in bending tensile stress at the top plate with frost heave amount is greater than that at the bottom plate. Further analysis indicates that when the wavelength is 6 m or 10 m, the stress values of the slab do not change significantly with frost heave amount. However, when the wavelength increases to 20 m, the stress at the bottom plate increases sharply with frost heave amount. This is because the frost valley causes voids below the base layer. When the wavelength is small, the

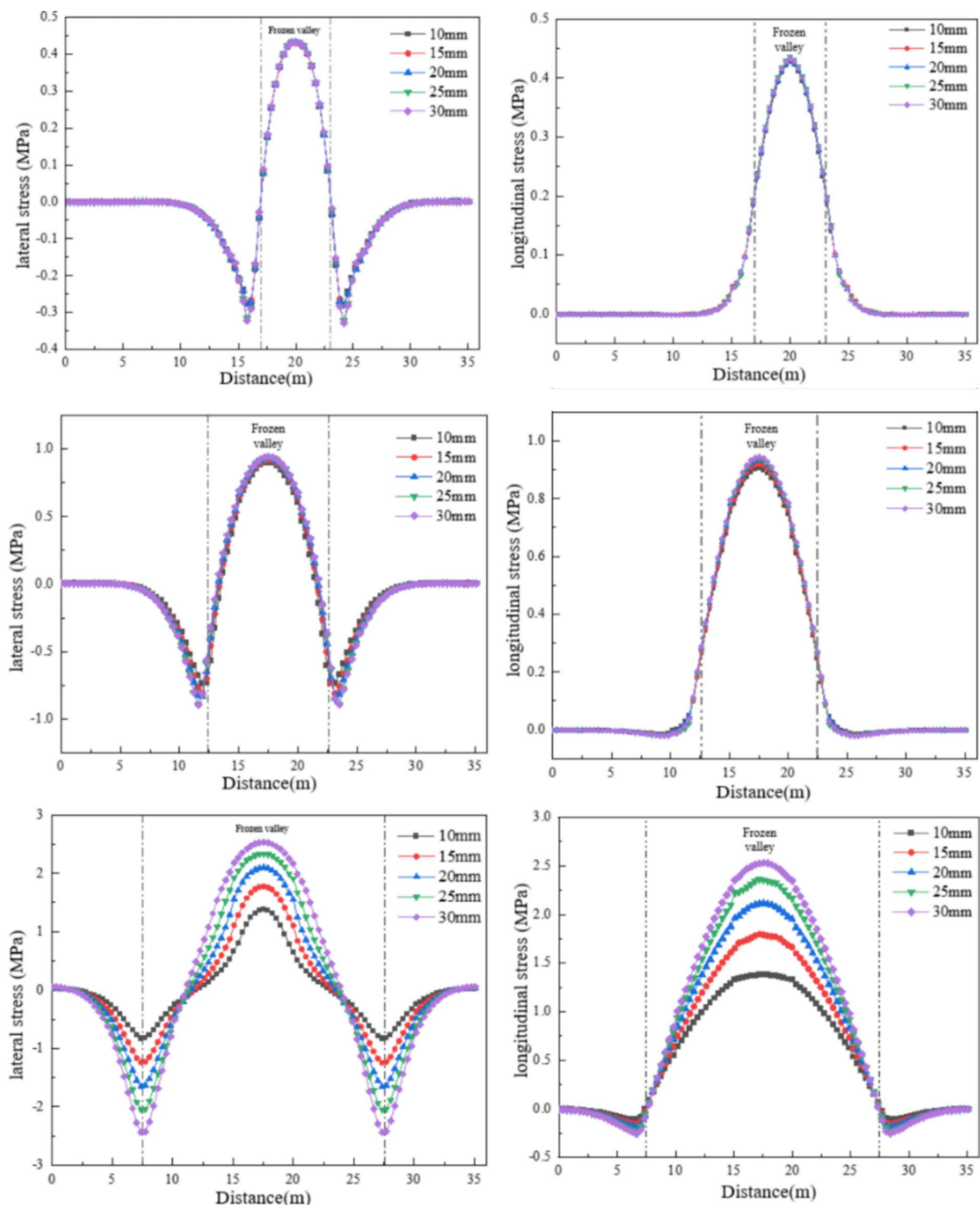


Fig. 13. Bottom plate horizontal stress (wavelength 6 m;10 m;20 m).

vertical strain of the pavement slab under gravity is limited and does not exceed the frost heave amount. As the wavelength increases, the vertical strain of the pavement slab increases with the frost heave amount, resulting in an increase in bending tensile stress at the bottom plate. This causes the pavement slab to behave similarly to a cantilever beam structure without support at the void, generating greater bending tensile stress at the top and bottom positions of the slab.

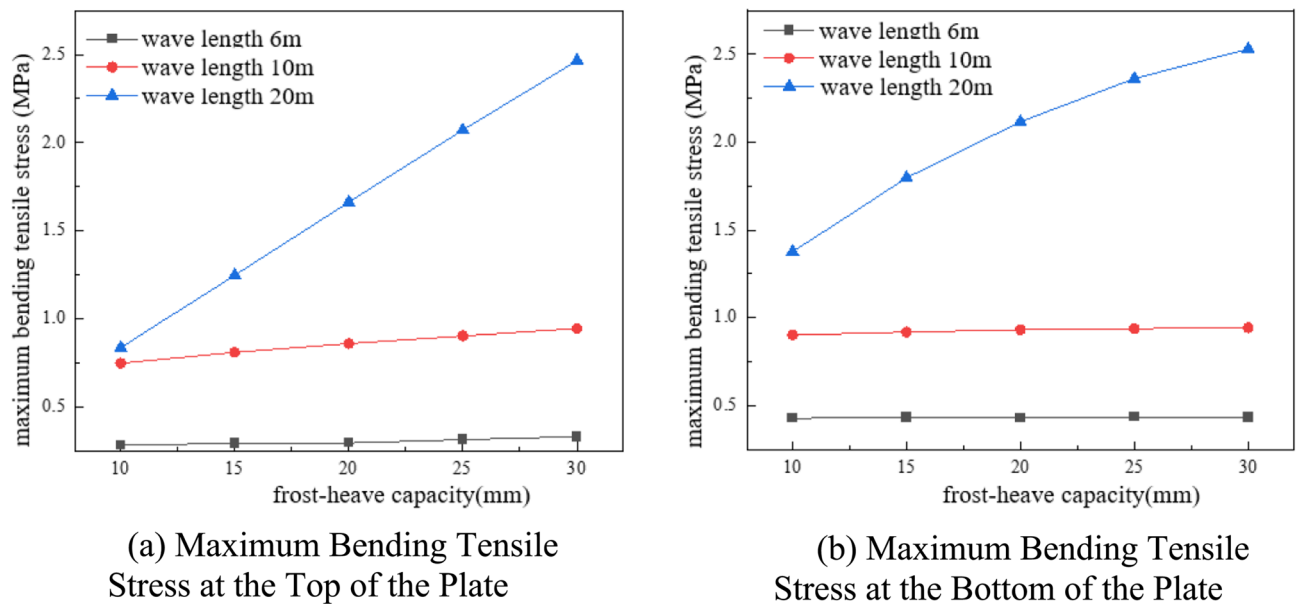


Fig. 14. Maximum bending tensile stress of the pavement.

Wavelength (m)	Figure number	Frost heave 10 mm	Frost heave 30 mm	Stress increment	growth rate
6	Figure 14(a)	0.283 MPa	0.330 MPa	0.047 MPa	+ 16.6%
	Figure 14(b)	0.428 MPa	0.433 MPa	0.005 MPa	+ 1.2%
10	Figure 14(a)	0.747 MPa	0.945 MPa	0.198 MPa	+ 26.5%
	Figure 14(b)	0.903 MPa	0.919 MPa	0.016 MPa	+ 1.8%
20	Figure 14 (a)	0.835 MPa	2.466 MPa	1.631 MPa	+ 195.3%
	Figure 14(b)	1.377 MPa	2.531 MPa	1.154 MPa	+ 83.8%

Table 4. Maximum bending tensile stress of the pavement.

Influence of frost heave wavelength on pavement stress

To study the influence of frost heave wavelength on pavement stress under self-weight, four wavelengths (6 m, 10 m, 15 m, 20 m) were selected, with each wavelength corresponding to three frost heave amounts (10 mm, 20 mm, 30 mm) for analysis. Summarize the data in the Fig. 15 into a Table 5.

Therefore, the bending tensile stress values of the pavement are positively correlated with the wavelength. Further analysis shows that when the frost heave amount is 10 mm, the growth rate of bending tensile stress at the top and bottom plates slows down with the increase in frost heave wavelength. This is because when the frost heave amount is small, the vertical displacement of the base layer is limited, providing support for the bottom of the surface layer, resulting in insignificant changes in bending tensile stress at the bottom of the surface layer.

Influence of frost heave amount and wavelength on pavement deformation

To investigate the influence of frost heave amount and wavelength on the vertical displacement of pavement, three frost heave morphologies were analyzed. The vertical displacement extraction path was consistent with the stress extraction path shown in Fig. 16. In Fig. 16(a), “6 m-10 mm” represents the frost valley morphology with a wavelength of 6 m and a frost heave amount of 10 mm. The maximum vertical displacement of the surface layer is 0.027 mm, and the maximum vertical displacement of the base layer is 0.332 mm. The displacement of the surface layer is slightly smaller than that of the base layer, and both are less than the frost heave amount of 10 mm, indicating the presence of a void below the base layer under gravity, with a slight void between the surface layer and the base layer.

In Fig. 16(b), the maximum vertical displacement of the surface layer is 7.097 mm, and the maximum vertical displacement of the base layer is 8.628 mm, indicating voids below both the surface layer and the base layer. In Fig. 16(c), the maximum vertical displacement of the surface layer is 3.657 mm, and the maximum vertical displacement of the base layer is 3.793 mm. The vertical displacements of the surface layer and the base layer are very close but do not exceed the frost heave amount of 5 mm, indicating a slight gap between the surface layer and the base layer, and voids below the base layer.

Comparing Fig. 16(a) and (b), the vertical displacement of the surface layer and the base layer increases with the increase in wavelength, and the gap between the base layer and the surface layer also increases. This is because the increase in wavelength is analogous to the increase in the length of the force arm of the simply

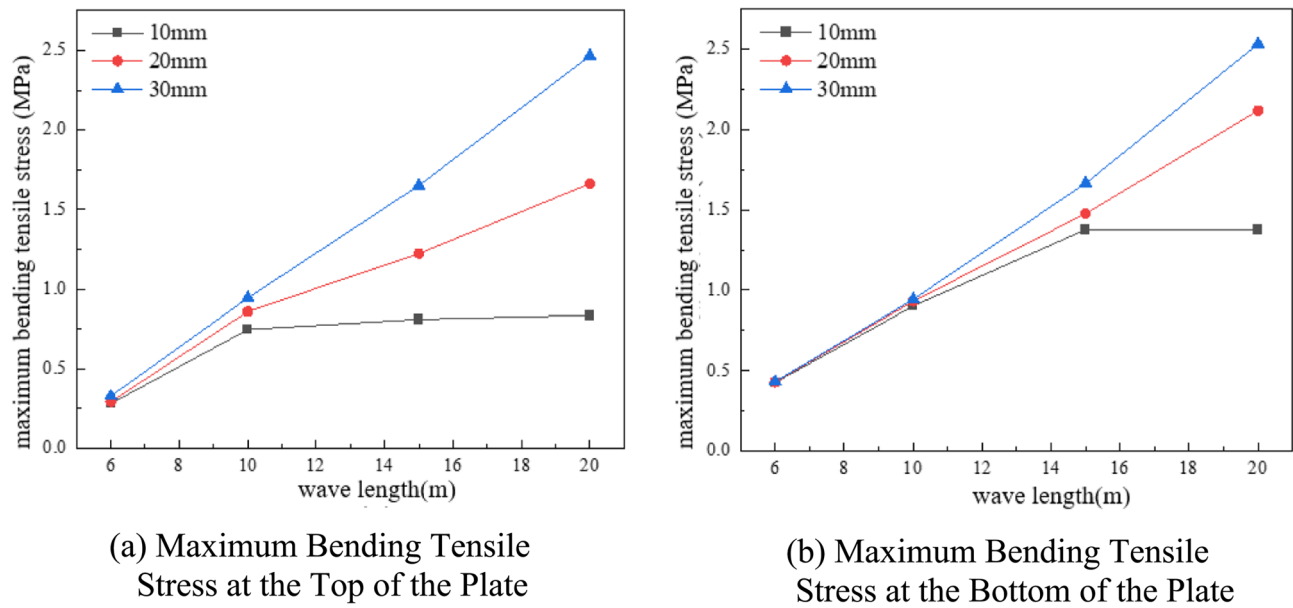


Fig. 15. Maximum bending tensile stress of the pavement.

Figure number	Frost heave amount	6 m wavelength stress	20 m wavelength stress	Stress increment	Growth rate (times)
Figure 15 (a)	10 mm	0.283 MPa	0.835 MPa	+ 0.552 MPa	1.951
	20 mm	0.294 MPa	1,663 MPa	+ 1.369 MPa	4.715
	30 mm	0.330 MPa	2,466 MPa	+ 2.136 MPa	6.473
Figure 15 (b)	10 mm	0.428 MPa	1,377 MPa	+ 0.949 MPa	2.217
	20 mm	0.431 MPa	1,117 MPa	+ 0.686 MPa	1.592
	30 mm	0.433 MPa	2,531 MPa	+ 2.098 MPa	4.845

Table 5. Maximum bending tensile stress of the pavement.

supported beam structure of the pavement slab, resulting in an increase in the deflection value of the surface layer and the base layer. However, the elastic modulus of the surface layer is greater than that of the base layer, so the deflection of the surface layer is smaller than that of the base layer. Comparing Fig. 16(b) and (c), the gap between the surface layer and the base layer and the void area below the surface layer increase with the increase in frost heave amount.

Influence of relative frost heave position on pavement mechanical behavior

Influence of relative frost heave position on pavement mechanical behavior.

This section selects three frost heave wavelengths (6 m, 10 m, 20 m) with a frost heave amount of 10 mm to analyze the influence of different relative frost heave positions on pavement stress. As shown in Fig. 17, the relative frost heave position mainly refers to the relative relationship between the frost peak and the slab joint, which can be divided into two situations: the frost peak is located at the slab joint, with the frost heave center located in the middle of the slab, and the frost peak is located in the middle of the slab, with the frost heave center located at the slab joint. As shown in Fig. 18, the relative error of the maximum bending tensile stress at the top plate under the two frost heave positions is 4.3% ~ 12.2%. As shown in Fig. 19, the relative error of the maximum bending tensile stress at the bottom plate is 2% ~ 13.8%. Overall, the bending tensile stress of the pavement does not change significantly with the relative frost heave position of the subgrade. This is because although the relative position of the frost heave changes with respect to the slab, according to the simply supported beam and cantilever beam structures, the frost heave wavelength remains constant, i.e., the length of the force arm does not change, and the frost heave morphology remains unchanged. Therefore, the stress on the pavement under self-weight does not change. In the case of voids at the bottom of the slab, the bending tensile stress at the bottom of the simply supported beam structure is mainly determined by the support conditions. If the boundary conditions (such as the support points of the simply supported beam) of the void area remain unchanged, the bending tensile stress distribution determined by these boundary conditions will also remain unchanged. Therefore, the stress changes in the base layer and the slab are not significant.

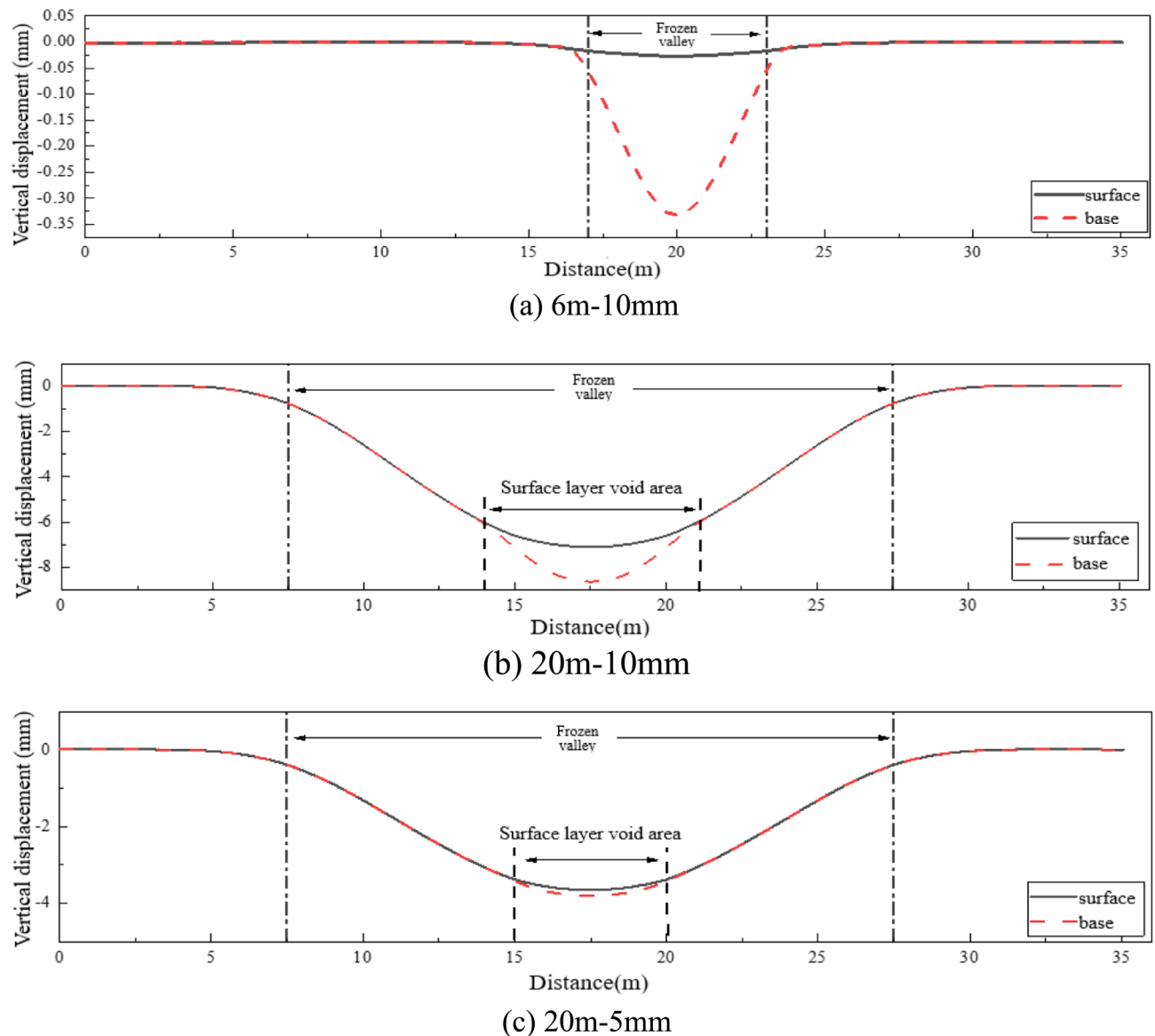


Fig. 16. Vertical displacement of surface and base layers.

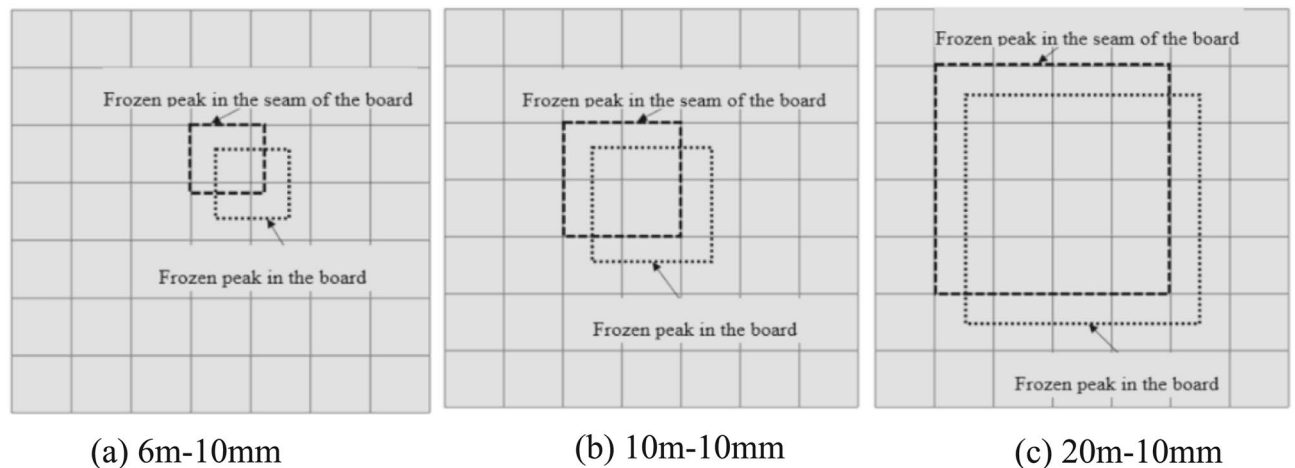


Fig. 17. Schematic diagram of different relative frost heave positions.

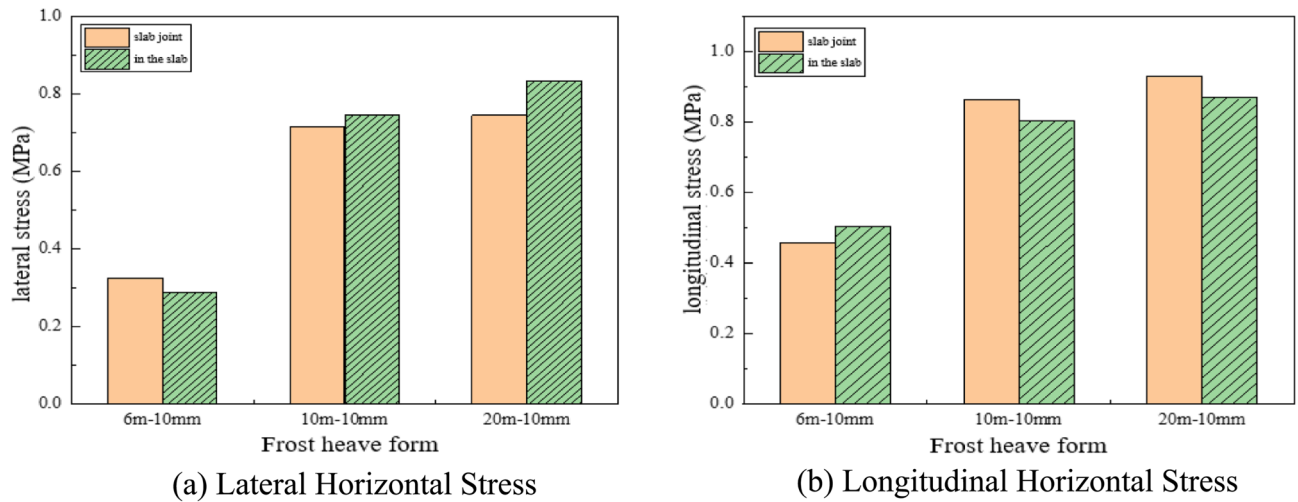


Fig. 18. Maximum bending tensile stress at the bottom of the plate.

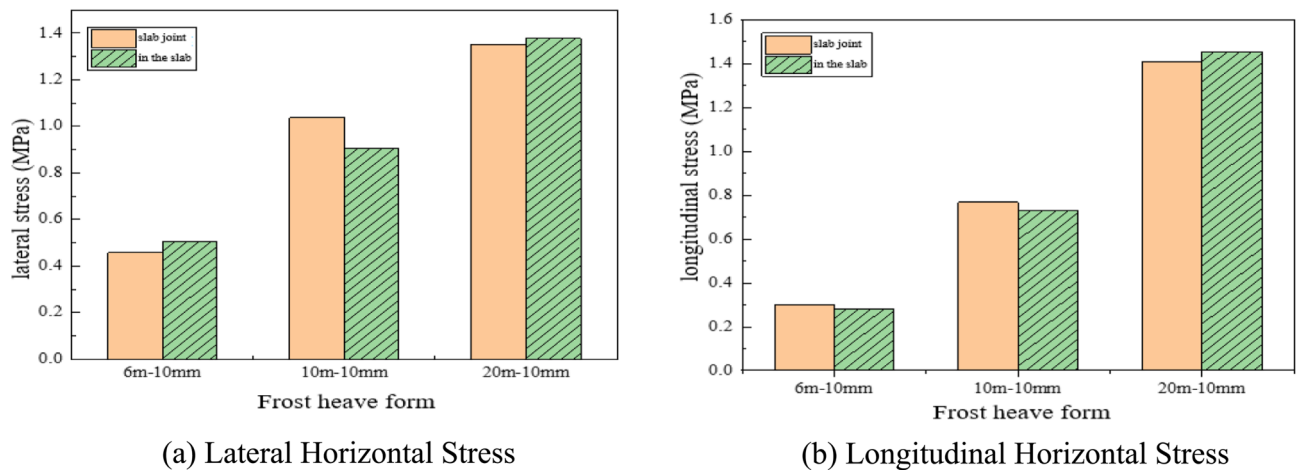


Fig. 19. Maximum bending tensile stress at the top of the plate.

Frost heave control indicators and standards for airport subgrades in seasonal frozen soil areas

In engineering practice, if the frost heave experienced by a cement concrete pavement exceeds the design limits, it may cause early damage such as longitudinal cracks, significantly affecting the functionality and service life of the pavement. Addressing the issue of pavement frost heave by designing pavement structures and thicknesses to eliminate uneven frost heave is not only costly but also lacks practical engineering rationality. Therefore, this study proposes control indicators for subgrade frost heave, aiming to provide a scientific basis for designing pavements based on the allowable frost heave of the pavement. The establishment of these control indicators is crucial for ensuring the normal operation and flight safety of airport runways under cold climate conditions.

Control indicators based on pavement mechanical behavior analysis

Fatigue stress calculation

Fatigue stress of a material refers to the phenomenon of material performance degradation and failure due to repeated stress application. Fatigue stress is one of the important parameters in the fatigue strength design of materials and is significant for evaluating the performance of materials under complex loads. In civil aviation transport airports, the fatigue of cement concrete pavement is a critical issue related to the operational safety and efficiency of the airport.

The design of cement concrete pavement structures should be based on the following standards: within the specified design service life, even under the combined action of aircraft load and temperature gradient, the surface layer slab should not experience fatigue cracking. For structural safety verification, it should be ensured that under the combined action of the heaviest axle load and the maximum temperature gradient, the pavement structure does not experience ultimate failure. The design and verification standards comprehensively

consider the impact of aircraft load and temperature changes on the pavement structure. The limit state design expressions can be respectively adopted as follows:

$$\gamma_r (\sigma_{pr} + \sigma_{tr}) \leq f_r \tag{33}$$

$$\gamma_r (\sigma_{p,max} + \sigma_{t,max}) \leq f_r \tag{34}$$

$$\gamma_r = 1 + \psi_1 + \psi_2 \tag{35}$$

In the formula:

- σ_{pr} —represents the load fatigue stress at the critical load position, in MPa;
- σ_{tr} —represents the temperature gradient fatigue stress at the critical load position, in MPa;
- $\sigma_{p,max}$ —represents the maximum load stress at the critical load position due to the heaviest axle load, in MPa;
- $\sigma_{t,max}$ —represents the maximum temperature warping stress at the critical load position due to the maximum temperature gradient in the region, in MPa;
- f_r —represents the standard value of the flexural tensile strength of cement concrete, in MPa;
- γ_r —represents the reliability coefficient;
- ψ_1 —represents the construction variability level coefficient, which can be taken as 0.05 to 0.36 based on the target reliability;
- ψ_2 —represents the material parameter determination level coefficient, which can be taken as 0 to 10% based on different levels.

According to airport specifications, for airports with flight area indicator II classified as A or B, the design strength standard for cement concrete pavement should be at least 4.5 MPa. For airports with flight area indicator II classified as C, D, E, or F, the design strength standard for cement concrete pavement should be higher, not less than 5.0 MPa. Considering safety, the construction variability level coefficient is taken as 0.2, and the material parameter determination level coefficient is taken as 5%. According to Eq. 31, the reliability coefficient is 1.25. According to Eq. 29, the sum of the load fatigue stress and the temperature gradient fatigue stress is recorded as the fatigue stress, as shown in Table 6.

In winter, as the atmospheric temperature drops to sub-zero levels, the temperature transmission within the various structural layers of the pavement exhibits a lag effect. Consequently, the temperature at the top of the slab is lower than at the bottom, resulting in a negative temperature gradient in the vertical direction of the slab. Under this negative temperature gradient, due to the effects of self-weight and constraints, temperature stress will be generated within the slab, causing warping deformation. The slab will curve upwards.

On one hand, in the case of subgrade frost heave, the slab will curve upwards, resulting in insufficient support at the bottom of the pavement slab, thereby creating a height difference (Δh) from its original position. Consequently, the permissible frost heave amount proposed based on the bending tensile stress and load fatigue stress derived from the simulation is smaller than the actual permissible frost heave amount.

On the other hand, if the temperature gradient fatigue stress is set to 0, the fatigue stress in Table 6 would be the load fatigue stress. Based on this, the proposed permissible frost heave amount for the subgrade would be larger than the actual permissible frost heave amount. This project considers the offset of the differences in both scenarios. Therefore, the permissible frost heave amount for the subgrade proposed based on the bending tensile stress and fatigue stress (with the temperature gradient fatigue stress set to 0) derived from the simulation is more consistent with the actual permissible frost heave amount.

Allowable frost heave amount of subgrade

Airport flight areas are classified according to Index I and Index II. The classification of airport flight areas by Index I and Index II is determined based on the characteristics of the aircraft intended to use the flight area. As shown in Table 7, Flight Area Index II is determined by the maximum wingspan of the various types of aircraft intended to use the runway in the flight area.

By the end of 2023, there were 259 transport airports within China. Certified transport airports are classified according to flight area indicators: 15 airports are classified as 4F, 39 as 4E, 37 as 4D, 163 as 4C, 4 as 3C, and 1 airport is below 3C. This indicates that most domestic transport airports have Flight Area Index II of C, D, E, or F. The aircraft models discussed in this project, B767-300ER, B747-400, and A380-800, operate at airports suitable for Flight Area Index II of C, D, E, or F. Therefore, this project mainly discusses the pavements of airports with Flight Area Index II of C, D, E, or F.

This article mainly discusses airport pavements with an Airfield Index II of C, D, E, or F, as these types of airport pavements are the most used. According to the maximum bending tensile stress at the bottom of the road surface of different aircraft models, as shown in Table 8. From the table, when the frost heave amount is 10 mm and 15 mm, the bottom stress of the slab for different aircraft models is generally below 4 MPa. When the frost

Airport pavement	Fatigue stress (MPa)
Flight area index II for A, B	3.6
Flight area index II for C, D, E, F	4

Table 6. Fatigue stress of cement concrete pavement.

Flight area index II	Wingspan(m)
A	<15
B	15 ~ 24(excluding)
C	24 ~ 36(excluding)
D	36 ~ 52(excluding)
E	52 ~ 65(excluding)
F	65 ~ 80(excluding)

Table 7. Flight area index II.

Frost heave amount(mm)	Models	Surface layer thickness(cm)	Surface layer modulus (GPa)	Base layer thickness(cm)	Base layer modulus (MPa)	Flexural tensile stress (MPa)
10	A380-800	25	36	40	1500	3.73
		30				3.63
		35				3.461
		40				3.341
		40	33			3.21
			34			3.244
			35			3.269
			37			3.424
		36	25	3.376		
				30		3.361
				35		3.354
			40	1300	3.353	
				1400	3.346	
				1600	3.335	
				1700	3.331	
	B767-300ER	1600	1.922			
	B747-400		2.828			
15	B767-300ER		2.072			
	B747-400		3.57			
	A380-800		4.097			
20	B767-300ER		2.265			
	B747-400		4.291			
	A380-800		4.937			
25	B767-300ER		2.484			
	B747-400		4.961			

Table 8. Maximum flexural tensile stress at the bottom of the pavement slab under static aircraft load.

heave amount increases to 20 mm and 25 mm, the bottom stress of the slab under the B767-300ER does not exceed 4 MPa, but under the A380-800, the bottom stress exceeds 4 MPa, which is greater than the pavement fatigue stress.

Compared to static loads, the slab bottom stress under dynamic loads from different aircraft types exhibits varying degrees of increase. Specifically, the B767-300ER aircraft shows no significant variation in slab bottom stress under dynamic loads, thus its dynamic load magnitude remains consistent with static loads. In contrast, the stress increases for the B747-400 and A380-800 aircraft are 18% and 21.16% respectively. Therefore, the bending tensile stress at the slab bottom under dynamic loads is presented in the table below.

By fitting the data of bending tensile stress and frost heave amount in Table 8 and Table 9 the fitting formula for the bending tensile stress and frost heave amount of the pavement under static aircraft loads is obtained, as shown in Table 10:

Based on the bending tensile stress in Table 2 and the fitting formulas in Table 10, the allowable frost heave amounts for the subgrade are obtained, as shown in Table 11.

During the taxiing-takeoff process, the aircraft's taxiing speed gradually increases, and the aircraft's lift increases accordingly. As a result, the longitudinal compressive stress and the lower tensile stress of the pavement slab gradually decrease. During the landing-taxiing process, the aircraft's taxiing speed gradually decreases. However, due to fuel consumption, the aircraft's weight at this time is about one-tenth less than its weight during takeoff. Therefore, during this process, the lower tensile stress on the pavement slab caused by the aircraft cannot

Frost heave (mm)	B767- 300ER	B747-400	A380-800
10	1.922	3.337	4.043
15	2.072	4.213	4.957
20	2.265	5.063	5.974
25	2.484	5.854	6.690

Table 9. The maximum bending tensile stress at the bottom of the track slab under the dynamic load of the aircraft(MPa).

Aircraft model		Fitting formula	R ²
B767-300ER	Static load	$y = 0.04x + 1.528$	0.990
B747-400	Static load	$y = 0.142x + 1.421$	0.999
A380-800	Static load	$y = 0.148x + 1.885$	0.993

Table 10. Fitting formulas for pavement bending tensile stress and frost heave amounts for different aircraft models.

Airport pavement		Allowable frost heave amount (mm)
Flight zone indicators A, B		20
Flight Zone Indicators C, D, E, F	With B767-300ER as Design Axle Load	Static Load61.8
	With B747-400 as Design Axle Load	Static Load18
	With A380-400 as Design Axle Load	Static Load14

Table 11. Subgrade frost heave standards based on mechanical impact.

reach the maximum bending tensile stress of the pavement simulated in this project under dynamic aircraft loads. Considering this comprehensively, this project ultimately proposes the allowable frost heave amount of the subgrade based on the bending tensile stress and fatigue stress of the pavement under static aircraft loads.

As shown in Table 11, due to the relatively small load of the B767-300ER aircraft, domestic airports rarely use the B767-300ER as the heaviest design axle load for the airport. Therefore, this project does not consider this aircraft type when discussing the allowable frost heave amount of the subgrade. For pavements with Flight Area Index II of C, D, E, F, using the B747-400 as the design axle load, the proposed allowable frost heave amount of the subgrade is 18 mm. Using the A380-400 as the design axle load, the proposed allowable frost heave amount of the subgrade is 14 mm. Since the A380-800 is currently the largest passenger aircraft in the world, and considering that most airports do not use the A380-400 as the design axle load, this project ultimately selects the intermediate value between the A380-800 and B747-400 as the standard for subgrade frost heave. Therefore, the allowable frost heave amount of the subgrade for pavements with Flight Area Index II of C, D, E, F is 15 mm.

For airports with Flight Area Index II of A, B, since the pavement structure of the airport, i.e., the thickness of the surface layer and the base layer, is similar to that of highway cement concrete pavement, and the design axle load of the airport is generally smaller than that of airports with Flight Area Index II of C, D, E, F, the allowable frost heave amount of the subgrade for airports with Flight Area Index II of A, B is proposed to be 20 mm, referencing the allowable frost heave amount of highways.

Safety precautions

During airport construction, strict attention must be paid to the uniformity of subgrade materials and compaction control. A minimum 50 cm uniform soil layer must be maintained beneath the frost protection layer to prevent differential frost heave caused by soil heterogeneity. Non-frost-susceptible materials such as sand-gravel mixtures should be utilized for construction, with stringent control of moisture content (e.g., silt moisture content must not exceed 25% below its liquid limit). Frost-susceptible materials should be cautiously avoided for subgrade applications.

Ground temperature sensors and frost heave markers should be deployed at airports, and melting and sedimentation deformation should be monitored in spring. If the frost heave is close to the allowable value (e.g. 14 mm), it needs to be repaired in advance. At the same time, the minimum antifreeze layer thickness should be adjusted according to the local freezing depth, soil quality and drainage conditions. For example, in a humid area with a freezing depth of 2.0 m, the frost protection layer of silt soil foundation is 0.9 ~ 1.5 m thick, but the lower limit can be removed if the drainage is optimized.

Conclusions

This study establishes a finite element model of airport rigid pavement incorporating subgrade frost heave morphology to simulate the mechanical response under various frost heave conditions. Based on the analysis of pavement behavior under self-weight, the following key conclusions and design recommendations are made:

Research findings

- (1) The most critical stress locations occur at the bottom of the slab above frost valleys and the top of the slab near the frost valley boundaries, with greater bending tensile stress often appearing at the slab bottom;
- (2) Pavement stress is positively correlated with frost heave amount—greater frost heave results in higher bending tensile stress;
- (3) When the frost heave wavelength is small, the increase in tensile stress with frost heave amount becomes less significant;
- (4) Pavement stress also increases with frost heave wavelength, particularly when frost heave amount is small;
- (5) The vertical separation between the surface and base layers increases with both wavelength and frost heave amount, leading to potential void formation beneath the slab;
- (6) The relative position of frost heave (e.g., peak vs. valley) has a limited impact on overall pavement stress, with the relative error of maximum top tensile stress ranging from 4.3% to 12.2%, and bottom tensile stress from 2% to 13.8%.

Design recommendations

Based on fatigue stress analysis and supporting literature, the allowable frost heave amounts for subgrade under airport rigid pavements are proposed as follows:

- (1) For flight area class II airports (Categories A and B): 20 mm
- (2) For flight area class II airports (Categories C, D, E, and F): 15 mm

These findings provide a scientific basis for defining frost heave limits in cement concrete pavements, supporting more standardized and reliable design and maintenance strategies for airport infrastructure.

Data availability

The datasets used and/or analysed during the current study available from the corresponding author on reasonable request.

Received: 21 May 2025; Accepted: 20 August 2025

Published online: 26 September 2025

References

1. Liu, J., Cen, G. & Chen, Y. Study on frost heaving characteristics of gravel soil pavement structures of airports in Alpine regions. *RSC Adv.* **7**, 24633–24642. <https://doi.org/10.1039/c7ra02151h> (2017).
2. Lenngren, C. Nondestructive evaluation of frost-heave effects on a runway. In *Presented at the nondestructive evaluation of aging aircraft, airports, and aerospace hardware II* (Eds. Geithman, G. & Georgeson, G.) 2–17 <https://doi.org/10.1117/12.305052> (1998).
3. Zaremotekhas, F., Hunsaker, A., Dave, E. & Sias, J. E. Development of an unpiloted aircraft system-based sensing approach to detect and measure pavement frost heaves. *J. Test. Eval.* **51**, 1953–1965. <https://doi.org/10.1520/JTE20220268> (2023).
4. Long, X., Cen, G., Cai, L. & Chen, Y. Model experiment of uneven frost heave of airport pavement structure on coarse-grained soils foundation. *Constr. Build. Mater.* **188**, 372–380. <https://doi.org/10.1016/j.conbuildmat.2018.08.100> (2018).
5. Lai, Y., Pei, W., Zhang, M. & Zhou, J. Study on theory model of hydro-thermal-mechanical interaction process in saturated freezing silty soil. *Int. J. Heat Mass Transf.* **78**, 805–819. <https://doi.org/10.1016/j.ijheatmasstransfer.2014.07.035> (2014).
6. Wang, Z. et al. Modeling temperature change and water migration of unsaturated soils under seasonal freezing-thawing conditions. *Cold Reg. Sci. Technol.* **218**, 104074. <https://doi.org/10.1016/j.coldregions.2023.104074> (2024).
7. Sun, L., Tang, X., Zeeman, B., Liu, Q. & Grasselli, G. Numerical investigation of the path-dependent frost heave process in frozen rock under different freezing conditions. *J. Rock Mech. Geotech. Eng.* **17**, 637–651. <https://doi.org/10.1016/j.jrmge.2024.02.031> (2025).
8. Teng, J., Liu, J., Zhang, S. & Sheng, D. Frost heave in coarse-grained soils: Experimental evidence and numerical modelling. *Geotechnique* **73**, 1100–1111. <https://doi.org/10.1680/jgeot.21.00182> (2022).
9. Cai, X., Liang, Y., Xin, T., Ma, C. & Wang, H. Assessing the effects of subgrade frost heave on vehicle dynamic behaviors on high-speed railway. *Cold Region. Sci. Technol.* **158**, 95–105. <https://doi.org/10.1016/j.coldregions.2018.11.009> (2019).
10. Ye, D. et al. The mechanics of frost heave with stratigraphic microstructure evolution. *Eng. Geol.* <https://doi.org/10.1016/j.enggeo.2023.107119> (2023).
11. Zhang, Y. et al. Experimental study on frost heave characteristics and micro-mechanism of fine-grained soil under dynamic load for heavy-haul railway subgrades in seasonally frozen regions. *Transp. Geotech.* <https://doi.org/10.1016/j.trgeo.2023.101146> (2023).
12. Hou, J. F., Zhang, R. Q. & Yu, J. Research on frost heaving of subgrade filling in seasonal frozen soil area. *AMR* **1065–1069**, 783–787. <https://doi.org/10.4028/www.scientific.net/AMR.1065-1069.783> (2014).
13. Lee, D. Y. & Kim, Y. C. A study of frost penetration depth and frost heaving in railway concrete track. *J. Korean Geoenviron. Soc.* **15**, 35–41. <https://doi.org/10.14481/jkges.2014.15.1.35> (2014).
14. Fattoev, U. B., Brushkov, A. V., Koshurnikov, A. V. & Gunar, A. Y. The frost heaving and heave properties of soils on the projected moscow-kazan railway. *Moscow Univ. Geol. Bull.* **76**(343), 351. <https://doi.org/10.3103/S0145875221030042> (2021).
15. Jin, D. et al. Performance of rubber modified asphalt mixture with tire-derived aggregate subgrade. *Constr. Build. Mater.* <https://doi.org/10.1016/j.conbuildmat.2024.138261> (2024).
16. Peng, L., Caiqian, Y., Fu, Xu., Junshi, Li. & Dongzhao, J. Reinforcement of insufficient transverse connectivity in prestressed concrete box girder bridges using concrete-filled steel tube trusses and diaphragms: A comparative study. *Building* **14**(8), 2466. <https://doi.org/10.3390/buildings14082466> (2024).
17. Guo, Y. & Zhai, W. Long-term prediction of track geometry degradation in high-speed vehicle-ballastless track system due to differential subgrade settlement. *Soil Dyn. Earthq. Eng.* **113**, 1–11. <https://doi.org/10.1016/j.soildyn.2018.05.024> (2018).

18. Liu, J., Yao, H. L., Chen, P. & Lu, Z. Dynamic response of subgrade under action of vehicle load considering pavement material roughness. *Mater. Res. Innov.* **18**, 966–970. <https://doi.org/10.1179/1432891714Z.000000000544> (2014).

Author contributions

C.H. and J.L. wrote the main manuscript text S.W. is responsible for submission.

Funding

The authors disclosed receipt of the following financial support for the research, authorship, and/or publication of this article: This work received funding from the following sources: National Natural Science Foundation of China (52472324). National Key Research and Development Program of China (2023YFC2907301). Key Scientific Research Project of the Ministry of Transport (2022-ZD4-039). Thank the above funds for their strong support for this study.

Declarations

Competing interests

The authors declare no competing interests.

Conflicting interests

The authors declared no potential conflicts of interest with respect to the research, authorship, and/or publication of this article.

Additional information

Correspondence and requests for materials should be addressed to S.W.

Reprints and permissions information is available at www.nature.com/reprints.

Publisher's note Springer Nature remains neutral with regard to jurisdictional claims in published maps and institutional affiliations.

Open Access This article is licensed under a Creative Commons Attribution-NonCommercial-NoDerivatives 4.0 International License, which permits any non-commercial use, sharing, distribution and reproduction in any medium or format, as long as you give appropriate credit to the original author(s) and the source, provide a link to the Creative Commons licence, and indicate if you modified the licensed material. You do not have permission under this licence to share adapted material derived from this article or parts of it. The images or other third party material in this article are included in the article's Creative Commons licence, unless indicated otherwise in a credit line to the material. If material is not included in the article's Creative Commons licence and your intended use is not permitted by statutory regulation or exceeds the permitted use, you will need to obtain permission directly from the copyright holder. To view a copy of this licence, visit <http://creativecommons.org/licenses/by-nc-nd/4.0/>.

© The Author(s) 2025